

AFRL-VA-WP-TR-2000-3026

**SELECT MEANS FOR DETERMINING
UNSTEADY AERODYNAMIC RESPONSE
CHARACTERISTICS FROM STATIC DATA**



GREGORY A. ADDINGTON, PH.D.

**AFRL/VACA
AIR VEHICLES DIRECTORATE
AIR FORCE RESEARCH LABORATORY
AIR FORCE MATERIEL COMMAND
WRIGHT-PATTERSON AFB, OH 45433-7521**

JUNE 2000

FINAL REPORT FOR 04/17/1998 – 09/30/1998

APPROVED FOR PUBLIC RELEASE; DISTRIBUTION UNLIMITED

**AIR VEHICLES DIRECTORATE
AIR FORCE RESEARCH LABORATORY
AIR FORCE MATERIEL COMMAND
WRIGHT-PATTERSON AIR FORCE BASE OH 45433-7542**

20001026 010


Unlimited, Statement A

NOTICE

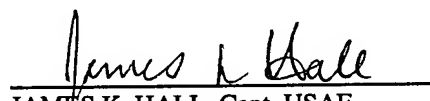
USING GOVERNMENT DRAWINGS, SPECIFICATIONS, OR OTHER DATA INCLUDED IN THIS DOCUMENT FOR ANY PURPOSE OTHER THAN GOVERNMENT PROCUREMENT DOES NOT IN ANY WAY OBLIGATE THE US GOVERNMENT. THE FACT THAT THE GOVERNMENT FORMULATED OR SUPPLIED THE DRAWINGS, SPECIFICATIONS, OR OTHER DATA DOES NOT LICENSE THE HOLDER OR ANY OTHER PERSON OR CORPORATION; OR CONVEY ANY RIGHTS OR PERMISSION TO MANUFACTURE, USE, OR SELL ANY PATENTED INVENTION THAT MAY RELATE TO THEM.

THIS REPORT IS RELEASABLE TO THE NATIONAL TECHNICAL INFORMATION SERVICE (NTIS). AT NTIS, IT WILL BE AVAILABLE TO THE GENERAL PUBLIC, INCLUDING FOREIGN NATIONS.

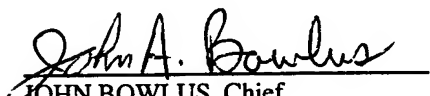
THIS TECHNICAL REPORT HAS BEEN REVIEWED AND IS APPROVED FOR PUBLICATION.



GREGORY A. ADDINGTON, Ph.D.
Project Engineer
Control Theory Optimization Branch



JAMES K. HALL, Capt, USAF
Chief, Control Theory Optimization Branch
Control Science Division



JOHN BOWLUS, Chief
Control Science Division
Air Vehicles Directorate

Do not return copies of this report unless contractual obligations or notice on a specific document require its return.

REPORT DOCUMENTATION PAGE			Form Approved OMB No. 0704-0188	
Public reporting burden for this collection of information is estimated to average 1 hour per response, including the time for reviewing instructions, searching existing data sources, gathering and maintaining the data needed, and completing and reviewing the collection of information. Send comments regarding this burden estimate or any other aspect of this collection of information, including suggestions for reducing this burden, to Washington Headquarters Services, Directorate for Information Operations and Reports, 1215 Jefferson Davis Highway, Suite 1204, Arlington, VA 22202-4302, and to the Office of Management and Budget, Paperwork Reduction Project (0704-0188), Washington, DC 20503.				
1. AGENCY USE ONLY (Leave blank)		2. REPORT DATE June 2000	3. REPORT TYPE AND DATES COVERED Final Report, 17 April 1998 to 30 September 1998	
4. TITLE AND SUBTITLE Select Means for Determining Unsteady Aerodynamic Response Characteristics from Static Data			5. FUNDING NUMBERS PE 62201F PR 2403 TA 05 WU 9L	
6. AUTHOR(S) Gregory A. Addington, Ph.D.				
7. PERFORMING ORGANIZATION NAME(S) AND ADDRESS(ES) Air Vehicles Directorate Air Force Research Laboratory Air Force Materiel Command Wright-Patterson AFB, OH 453433 POC: Gregory A. Addington, AFRL/VACA, (937) 255-8490			8. PERFORMING ORGANIZATION REPORT NUMBER	
9. SPONSORING/MONITORING AGENCY NAME(S) AND ADDRESS(ES) Air Vehicles Directorate Air Force Research Laboratory Air Force Materiel Command Wright-Patterson AFB, OH 453433 POC: Gregory A. Addington, AFRL/VACA, (937) 255-8490			10. SPONSORING/MONITORING AGENCY REPORT NUMBER AFRL-VA-WP-TR-2000-2036	
11. SUPPLEMENTARY NOTES				
12a. DISTRIBUTION AVAILABILITY STATEMENT Approved for public release; distribution unlimited.			12b. DISTRIBUTION CODE	
13. ABSTRACT (Maximum 200 words) Recent analysis has shown that nearly every high-performance tactical aircraft in the inventory of American and allied air forces has experienced some sort of unexpected controlled-flight departure in the early stages of flight testing. Most, if not all, of these in-flight departures had characteristics which lead to the conclusion that they were the result of critical state encounters. Critical states are discrete flight mechanical state vector values where the aerodynamic response loses its analytic dependence on one or more of the variables in that state vector. Critical states manifest themselves as discontinuities in either magnitude or slope in static force and moment data, and as dynamic responses which may be nonlinear with respect to either geometric parameters and/or time. This report presents two analysis procedures which have shown promise in the detection of critical states. First, spectral analysis of data ensembles acquired during wind tunnel tests of two 65° delta wings has shown that changes in these spectra signal the presence of some critical states. Further, the nature of these spectra have in some instances provided insight into the nature of the dynamic response. The second analysis procedure involves comparing the static experimental data to a simple potential-flow-based numerical model. It was found that when the experimental dataset diverged from the numerical simulation, critical states were present. Both of these analysis procedures required no additional data to be acquired and minimal analytical effort. Therefore, they provide a cost-effective means for adverting the effects of critical states during early air vehicle test-and-evaluation programs.				
14. SUBJECT TERMS Nonlinear dynamics, stability and control, aerodynamic modeling, wind tunnel testing, data analysis, high angle of attack aerodynamics			15. NUMBER OF PAGES	
			16. PRICE CODE	
17. SECURITY CLASSIFICATION OF REPORT UNCLASSIFIED	18. SECURITY CLASSIFICATION OF THIS PAGE UNCLASSIFIED	19. SECURITY CLASSIFICATION OF ABSTRACT UNCLASSIFIED	20. LIMITATION OF ABSTRACT UL	

GENERAL INSTRUCTIONS FOR COMPLETING SF 298

The Report Documentation Page (RDP) is used in announcing and cataloging reports. It is important that this information be consistent with the rest of the report, particularly the cover and title page. Instructions for filling in each block of the form follow. It is important to *stay within the lines* to meet *optical scanning requirements*.

Block 1. Agency Use Only (Leave blank).

Block 2. Report Date. Full publication date including day, month, and year, if available (e.g. 1 Jan 88). Must cite at least the year.

Block 3. Type of Report and Dates Covered. State whether report is interim, final, etc. If applicable, enter inclusive report dates (e.g. 10 Jun 87 - 30 Jun 88).

Block 4. Title and Subtitle. A title is taken from the part of the report that provides the most meaningful and complete information. When a report is prepared in more than one volume, repeat the primary title, add volume number, and include subtitle for the specific volume. On classified documents enter the title classification in parentheses.

Block 5. Funding Numbers. To include contract and grant numbers; may include program element number(s), project number(s), task number(s), and work unit number(s). Use the following labels:

C - Contract	PR - Project
G - Grant	TA - Task
PE - Program Element	WU - Work Unit Accession No.

Block 6. Author(s). Name(s) of person(s) responsible for writing the report, performing the research, or credited with the content of the report. If editor or compiler, this should follow the name(s).

Block 7. Performing Organization Name(s) and Address(es). Self-explanatory.

Block 8. Performing Organization Report Number. Enter the unique alphanumeric report number(s) assigned by the organization performing the report.

Block 9. Sponsoring/Monitoring Agency Name(s) and Address(es). Self-explanatory.

Block 10. Sponsoring/Monitoring Agency Report Number. (If known)

Block 11. Supplementary Notes. Enter information not included elsewhere such as: Prepared in cooperation with....; Trans. of....; To be published in.... When a report is revised, include a statement whether the new report supersedes or supplements the older report.

Block 12a. Distribution/Availability Statement.

Denotes public availability or limitations. Cite any availability to the public. Enter additional limitations or special markings in all capitals (e.g. NOFORN, REL, ITAR).

DOD - See DoDD 5230.24, "Distribution Statements on Technical Documents."

DOE - See authorities.

NASA - See Handbook NHB 2200.2.

NTIS - Leave blank.

Block 12b. Distribution Code.

DOD - Leave blank.

DOE - Enter DOE distribution categories from the Standard Distribution for Unclassified Scientific and Technical Reports.

NASA - Leave blank.

NTIS - Leave blank.

Block 13. Abstract. Include a brief (*Maximum 200 words*) factual summary of the most significant information contained in the report.

Block 14. Subject Terms. Keywords or phrases identifying major subjects in the report.

Block 15. Number of Pages. Enter the total number of pages.

Block 16. Price Code. Enter appropriate price code (*NTIS only*).

Blocks 17. - 19. Security Classifications. Self-explanatory. Enter U.S. Security Classification in accordance with U.S. Security Regulations (i.e., UNCLASSIFIED). If form contains classified information, stamp classification on the top and bottom of the page.

Block 20. Limitation of Abstract. This block must be completed to assign a limitation to the abstract. Enter either UL (unlimited) or SAR (same as report). An entry in this block is necessary if the abstract is to be limited. If blank, the abstract is assumed to be unlimited.

Table of Contents

Table of Contents.....	i
Nomenclature.....	v
1.0 Introduction	1
2.0 Wind Tunnel Experiments	5
2.1 SARL Experiments	5
2.2 University of Notre Dame Experiments	6
3.0 Spectral Analysis	7
3.1 SARL Data	7
3.2 Spectral Analysis - Theoretical Basis	7
3.3 HCAR Experiment	8
3.4 Discussion of Results.....	17
3.5 Summary.....	18
4.0 Static Slope Analysis	19
4.1 Calculation of Potential and Vortical Flow Contributions in the Experimental Data	19
4.2 Calculation of the Numerical Prediction	19
4.3 Correlation Between Experimental and Numerical Static Slopes	19
4.4 Correlation of Static Slope Comparability and Critical State Locations	22
4.5 Discussion of Results.....	24
4.6 Extrapolation of Results to Other Flows	25
4.7 Summary.....	27
5.0 Conclusions and Recommendations	28
6.0 References	29

List of Figures

Figure 1 Static rolling moment coefficient data as a function of body-axis roll angle for a 65° delta wing with center body; time constants from Myatt.	2
Figure 2 Unsteady rolling moment time histories in response to a ramp-and-hold maneuver of a 65° delta wing in the SARL wind tunnel. $U_\infty = 100\text{m/s}$, $\sigma = 30^\circ$. ⁸	3
Figure 3 A schematic of the 65° delta wing used in the SARL wind tunnel.	5
Figure 4 A schematic of the 65° delta wing used in the HCAR wind tunnel.	6
Figure 5 PSD results for SARL rolling moment data: ⁹ a) $\sigma = 30^\circ$, $\phi = 20^\circ$; b) $\sigma = 30^\circ$, $\phi = 5^\circ$	7
Figure 6 Static rolling moment coefficient as a function of roll angle with full-range regression results, $\sigma = 25^\circ$	9
Figure 7 Static rolling moment coefficient as a function of roll angle with full-range regression results, $\sigma = 30^\circ$	10
Figure 8 Static rolling moment coefficient as a function of roll angle with full-range regression results, $\sigma = 35^\circ$	10
Figure 9 Static rolling moment coefficient as a function of roll angle showing critical state locations and unsteady response time constants, $\sigma = 25^\circ$	10
Figure 10 Static rolling moment coefficient as a function of roll angle showing critical state locations and unsteady response time constants, $\sigma = 30^\circ$	11
Figure 11 Static rolling moment coefficient as a function of roll angle showing critical state locations and unsteady response time constants, $\sigma = 35^\circ$	11
Figure 12 Power spectral density decomposition of time series rolling moment data,	12
Figure 13 Power spectral density decomposition of time series rolling moment data,	13
Figure 14 Power spectral density decomposition of time series rolling moment data,	13
Figure 15 Integrated low-frequency PSD results, $\sigma = 25^\circ$	14
Figure 16 Integrated low-frequency PSD results, $\sigma = 30^\circ$	15
Figure 17 Integrated low-frequency PSD results, $\sigma = 35^\circ$	16
Figure 18 Static rolling moment data from the SARL wind tunnel with the potential flow prediction, critical state locations and unsteady-response time constants. $U_\infty = 100\text{ m/s}$, $\sigma = 30^\circ$	20

Figure 19 Static rolling moment data from the University of Notre Dame wind tunnel with the potential flow prediction, critical state locations and unsteady-response time constants. $U_\infty = 14.7$ m/s, $\sigma = 25^\circ$	21
Figure 20 Static rolling moment data from the University of Notre Dame wind tunnel with the potential flow prediction, critical state locations and unsteady-response time constants. $U_\infty = 14.7$ m/s, $\sigma = 30^\circ$	21
Figure 21 Static rolling moment data from the University of Notre Dame wind tunnel with the potential flow prediction, critical state locations and unsteady-response time constants. $U_\infty = 14.7$ m/s, $\sigma = 35^\circ$	22
Figure 22 A notional comparison of the static lift generated by a thin two-dimensional airfoil compared to a potential flow prediction.	26
Figure 23 A notional example of the dynamic lift generated by a harmonically-oscillating two-dimensional airfoil.	27

Nomenclature

AFRL	Air Force Research Laboratory
b	trailing-edge wing span (m)
c	root-chord length (m)
Δt	event time scale
f	frequency
HCAR	Hessert Center for Aerospace Research
IAR	Institute for Aerospace Research (Canada)
LEV	leading-edge vortex
NIR	Nonlinear Indicial Response
P	non-dimensional roll rate, $\dot{\phi} b/2U$
PSD	power-spectral density
RMS	root mean square
SARL	Subsonic Aerodynamics Research Laboratory
t	time reference (sec)
U	freestream velocity (m/sec)
ϕ	body-axis roll angle (deg)
$\dot{\phi}$	body-axis roll rate (rad/sec)
σ	body-axis angle of attack (deg)
τ	time constant, $2tU/b$

1.0 Introduction

The need for nonlinear flight mechanics models has increased as aircraft – particularly combat aircraft – have been designed to take increasing advantage of high angle-of-attack flight, vortex lift and other conditions where the aerodynamic response's (approximate) linearity with respect to the vehicle's maneuver state is lost. However, the ability to predict at what conditions this assumption of linearity is valid and where it is violated has not matured sufficiently as to be incorporated into an acceptable engineering tool. Instead, the aircraft design, test and evaluation communities have continued to rely on linear methods for modeling the entire envelope including those conditions where linear methods are invalid. Such limitations have become apparent as aircraft unexpectedly encounter phenomena such as wing rock, wing drop and nose slice. Indeed, a recent historical review¹ has shown that nearly every high-performance tactical aircraft in the inventory of American and allied air forces has experienced some sort of unexpected controlled-flight departure in the early stages of flight testing.

As a part of an effort to define high-fidelity models of nonlinear aerodynamic responses for use in flight simulation and control law design, a 65° delta wing configuration was tested at moderate to high angles-of-attack to develop a database for model testing and verification.^{2,3} Although these data were anticipated to contain nonlinearities, the degree of the nonlinearity was surprising; indeed, a number of *discontinuities* were found in these data.

In the analysis of these data, the Nonlinear Indicial Response (NIR) theory^{4,5,6} has proven quite useful. This model not only includes motion history effects in its modeling of responses to body motions, but also provides for the existence of discrete states where the aerodynamic response loses its analytic dependence on the motion variable(s). At these locations, known as critical states, discontinuities either in value or slope in the static data may be expected. Further, critical states can mark the boundary between flight regimes which have contrasting dynamic response characteristics, *e.g.*, dynamic responses which depend on frequency to varying degrees. The crossing of a critical state under dynamic conditions may be expected to introduce a transient component to the aerodynamic response. These behaviors appear as the result of the flow field topology undergoing a bifurcation and seeking a new and stable equilibrium structure.⁷

An example of static rolling moment data which contain critical states for the 65° delta wing is shown in Fig. 1. These data were acquired as a part of the IAR-AFRL joint research program,^{2,3} which was tasked to investigate this type of aerodynamic phenomena. They were collected at a body-axis angle of attack (σ) of 30° and freestream Mach number of 0.3 ($Re = 2.4$ million based on mean aerodynamic chord, $U_\infty = 100$ m/s). The most obvious of these critical states appeared at $\phi \approx \pm 5^\circ$, where the static rolling moment underwent a discrete jump in magnitude. The remaining two critical states, at $\phi \approx 7^\circ$ and 13° , the static rolling moment changes slope discontinuously. Pitching moment and normal force discontinuities at these same roll angles, coupled with regression analysis which failed to find a continuous function which could fit these data, reinforced these findings.

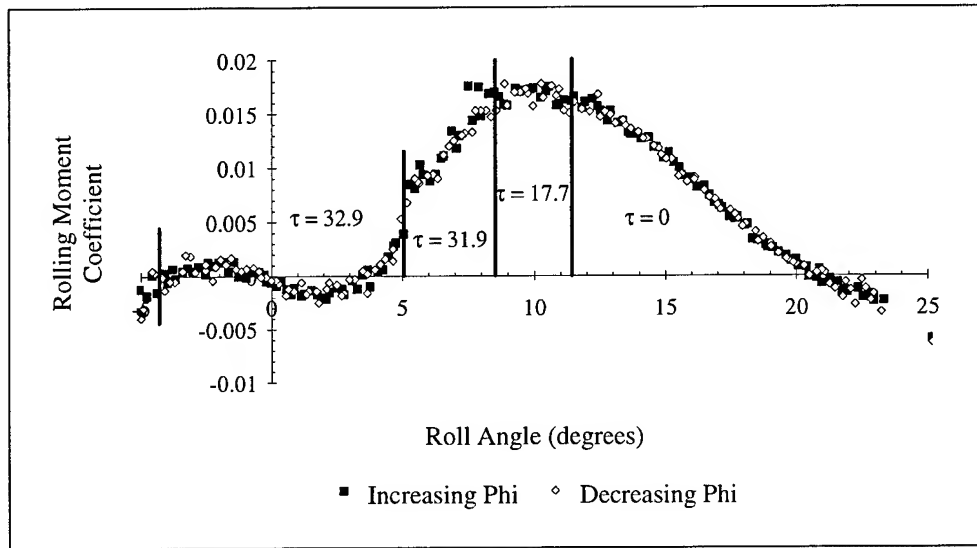


Figure 1 Static rolling moment coefficient data as a function of body-axis roll angle for a 65° delta wing with center body; time constants from Myatt.⁸

For the analysis of forced unsteady rolling moment data, Myatt⁸ developed a lagged-network-based state-space model. This numerical model contained a lagged-response component which could be approximately described as exponentially-decaying with a time constant of τ . Both Myatt⁸ and Addington⁷ demonstrated that by limiting single-degree-of-freedom body-axis-roll motions of a 65° delta wing configuration to ranges of roll angles which did not include critical states,^{9,10} the time constants remained relatively constant regardless of motion rate, direction or amplitude. The values of these time constants for the SARL database are shown in the appropriate regions in Figure 1. Figure 2 presents data which demonstrate slow temporal response characteristics and the results of applying Myatt's model. These data were acquired during ramp-and-hold body-axis-roll (ϕ) maneuvers of a 65° delta wing conducted at a body-axis angle of attack (σ) of 30° and freestream Mach number of 0.3 (the same conditions as those used for the static data shown in Figure 1). The unsteady rolling moment data clearly did not track the quasi-static data, instead requiring over 30 convective time units ($c_{root}/2U$) to reach the final equilibrium value.⁸

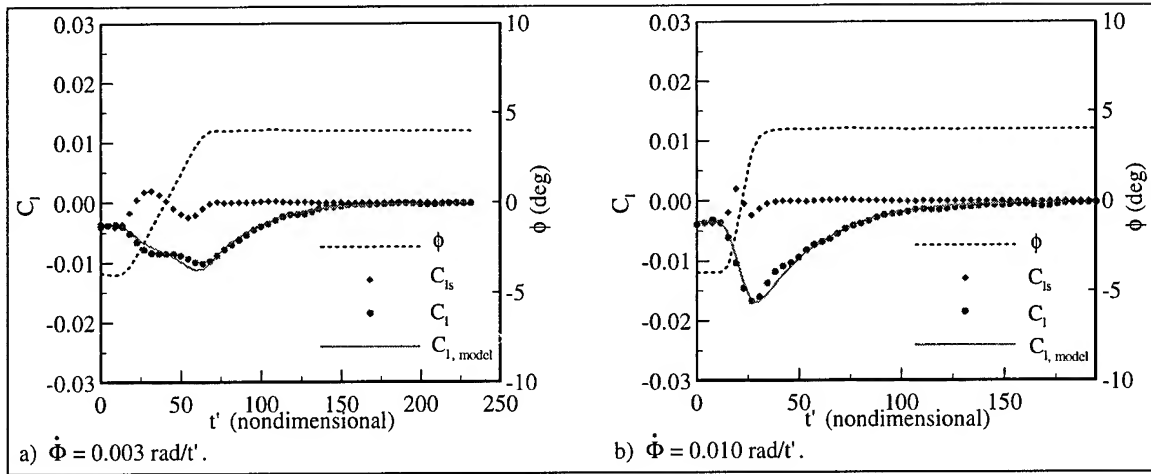


Figure 2 Unsteady rolling moment time histories in response to a ramp-and-hold maneuver of a 65° delta wing in the SARL wind tunnel. $U_\infty = 100\text{m/s}$, $\sigma = 30^\circ$.⁸

Of even greater interest were trends in these data which suggest that the unsteady response contained multiple time scales. The initial trend of these data was away from the quasi-static curve. Moreover, this trend initiated immediately following the initiation of the roll maneuver. This trend suggests that one component of the response reacted quickly with the changing maneuver state. Once the maneuver had terminated, the initial trend was reversed, and the rolling moment response decayed to its equilibrium value. This slow decay suggests a second component with a much slower response time scale. Grismer and Jenkins¹¹ first demonstrated that this "lagged" component could be accurately characterized by an exponential decay model, thus giving a measurable time constant.

This overall approach, although successful, is too expensive and time consuming for use in the average test-and-evaluation wind tunnel test. To date, only a small number of conditions have been thoroughly examined during the course of the IAR-AFRL research program, spanning several wind tunnel entries which have cumulatively consumed hundreds of testing hours. In addition, it can be difficult to differentiate between noise or random variations in the data and true discontinuities. (This difficulty is usually mitigated through the regression analysis of the static data and consideration of changes in the unsteady aerodynamic response characteristics.) Searching for changes in the flow topology, either through surface flow visualization, smoke visualization other means also may aid in locating critical states but add to the complication and costs of the wind tunnel entry.

Because of the expense involved in such high-resolution wind tunnel test matrices, it is desirable to find an alternative means of detecting critical states. Optimally, such a means ought to have minimal impact on traditional testing methods yet signal locations or regions of the envelope where additional attention ought to be paid, either through more comprehensive static testing or through dynamic testing, in order to avoid the potentially adverse critical state effects which may cause difficulties in actual flight operations. Recent analysis has shown that two off-line data analysis methods hold considerable promise in the detection of critical states.

The first of these methodologies is the spectral analysis of data ensembles. Static wind tunnel data is often taken by collecting a number of measurements of the aerodynamic forces and moments then averaging those data to arrive at a statistically-sound estimate for the actual static

data. This procedure is done to "average-out" experimental noise and any random unsteadiness which is a part of any wind tunnel test. However, as will be described in a following section, by decomposing these ensembles through spectral analysis, critical states may be located. Furthermore, the nature of these spectra may provide some insight into the nature of the way which the associated flow bifurcation alters the dynamic response of the air vehicle.

The second of these methodologies involves comparing the experimental data to potential-flow models of the relevant aerodynamics. Such a comparison, if valid, will yield conditions where the model and experimental data compare favorably and others where the two diverge. It is these divergence locations where critical states likely reside. Data supporting this assertion are also presented in this report.

2.0 Wind Tunnel Experiments

Data supporting the analyses discussed in this report were acquired in two separate wind tunnels: the AFRL Subsonic Aerodynamics Research Laboratory (SARL) located at Wright-Patterson AFB, OH; and the Hessert Center for Aerospace Research (HCAR) low-speed wind tunnels on the campus of the University of Notre Dame. These experiments are described separately below.

2.1 SARL Experiments

Experimental force and moment data of unprecedented comprehensiveness were collected for a 65° delta wing in the SARL wind tunnel. These experiments have been extensively described by previous authors (*c.f.*, References 2 and 3).

The SARL wind tunnel is a 7 ft – by – 10 ft open-return, low-turbulence wind tunnel. The model was mounted in the test section using an aft-mounting sting attached to an all-moving pitch sector. For the static experiments, the sting was a simple hollow steel shaft which attached directly to the internal six-component force balance. Dynamic roll experiments were conducted by replacing this sting with a purpose-built driven by a computer-controlled hydraulic servo motor. Dynamic pitch experiments required the replacement of the entire model support structure with a purpose-built pitch rig.

The 65° delta wing model (see Figure 3) was constructed of lightweight composites over a foam core. A wedge was included along the root chord over most of the model's length for stiffening. The combination of lightweight construction and structural stiffening enabled this model to undergo high-rate dynamic testing without fear of inertial deformation. All edges were coplanar and symmetrically beveled to a 20° included angle, so the model included no camber or twist. The circular center body housed the internal strain-gauge force balance.

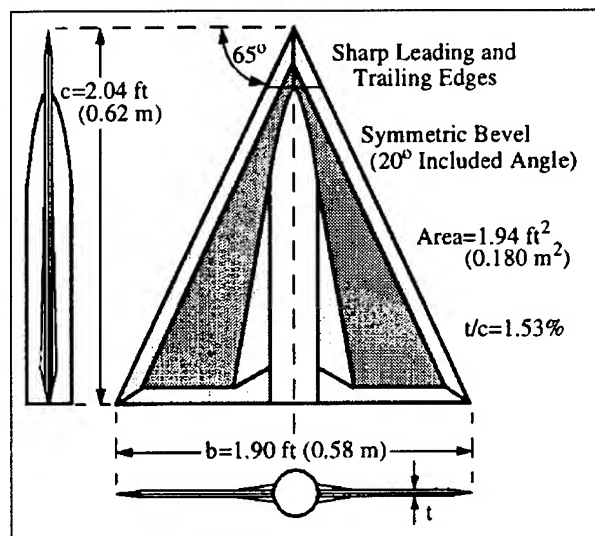


Figure 3 A schematic of the 65° delta wing used in the SARL wind tunnel.

The majority of SARL testing (including the data discussed herein) was conducted at a freestream Mach number of 0.3 ($Re = 2.4$ million based on mean aerodynamic chord, $U_\infty = 100$ m/s). Static and dynamic rolling experiments were conducted with a body-axis angle of attack fixed at 30° , with body-axis roll angles and rates set using the model support or dynamic test rig.

2.2 University of Notre Dame Experiments

Comprehensive static force and moment measurements were made using a smaller 65° delta wing model in the HCAR low-speed wind tunnel facilities. These experiments were comprehensively described in Reference 7. The delta wing model was an approximate one-half-scale replica of that used in the IAR-AFRL test program; a scale drawing is provided in Figure 4. The wind tunnels used are of a low-turbulence¹² ($<0.01\%$), open-return design with a 0.6 m - square test section. The model was mounted in the test section using an aft-mounted sting. The sting fixed the body-axis angle of attack and gave one-degree-of-freedom body-axis roll displacements controlled by an electric servo motor.

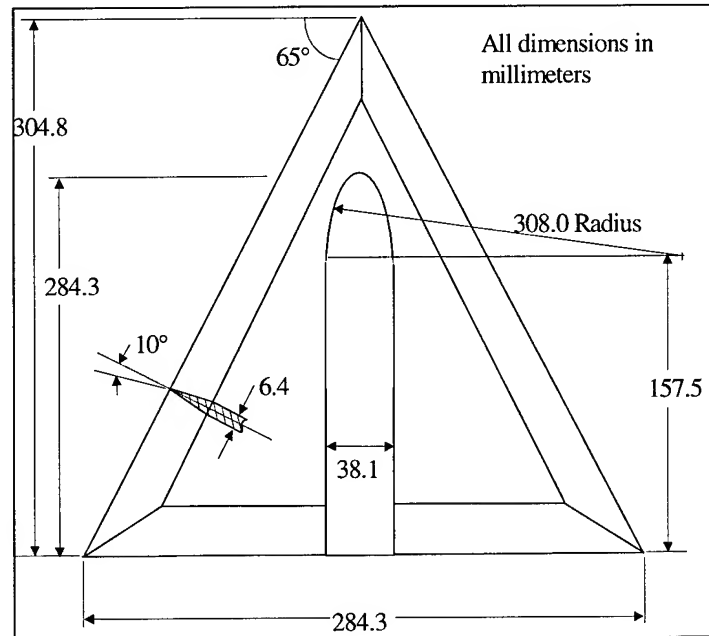


Figure 4 A schematic of the 65° delta wing used in the HCAR wind tunnel.

Force and moment measurements were made using a five-component internal strain-gauge force balance, located within the circular center body. The output signal was routed through a signal conditioner which provided both gain ($1000\times$) and low-pass filtering (1000 Hz cut-off frequency). These signals were sampled at 250 Hz for 20 seconds by a PC-based 16-bit analog-to-digital data acquisition system.

Static force and moment measurements were conducted with a freestream velocity of 14.7 m/s, giving a Reynolds number of 290,000 based on root chord. Body-axis angles of attack of 25° , 30° and 35° and roll angles from -20° to 90° were tested.

3.0 Spectral Analysis

3.1 SARL Data

Frequency analysis of analog data acquired during the 1993 SARL static wind tunnel entry demonstrated different spectral characteristics at different roll angles.⁹ Examples of these results are shown in Figure 5. In Figure 5a, a PSD of data acquired at $\sigma = 30^\circ$, $\phi = 20^\circ$ showed that the data contained no coherent low-frequency components ($f b / 2U \ll 1$) which were significantly elevated over the background noise. In contrast, data from $\sigma = 30^\circ$, $\phi = 5^\circ$ (Figure 5b) did show a very-low-frequency component which was significantly elevated over the background noise. This difference was attributed to the presence of LEV burst over the planform. From Figure 1 note also that the time constant was fast when the spectra showed no elevated low-frequency components and was slow when those components were elevated over the background noise. A hypothesis, based in part on this observation, is discussed in the following section.

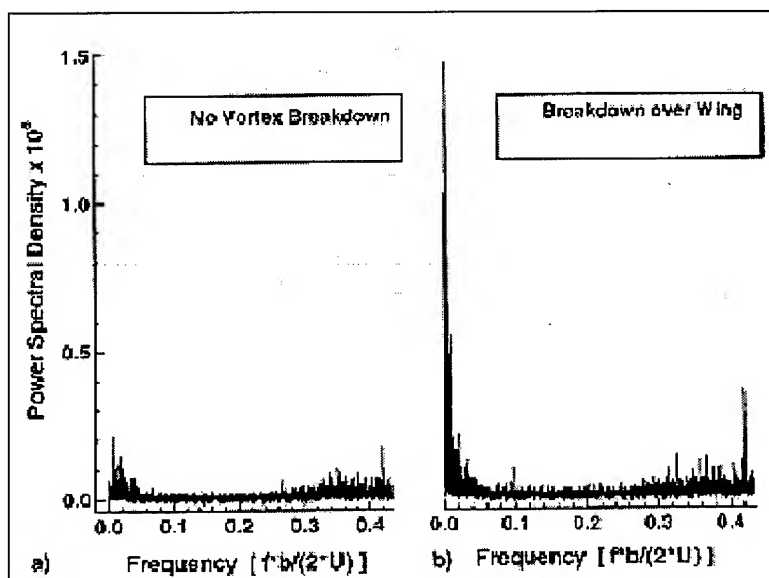


Figure 5 PSD results for SARL rolling moment data:⁹ a) $\sigma = 30^\circ$, $\phi = 20^\circ$; b) $\sigma = 30^\circ$, $\phi = 5^\circ$.

In the more recent HCAR wind tunnel experimental program, time histories of the aerodynamic response data were periodically recorded to further explore any relationship which may exist between critical states and changes in the frequency spectrum of the static loads. These results will be discussed following a review of the theoretical rationale of this analysis.

3.2 Spectral Analysis - Theoretical Basis

In Rockwell's review¹³ of the flow fields generated by delta wings at high angles of attack, the multiple-time-scale nature of these flows was discussed. These time scales may be divided into two main subsets: those which are comparable to or faster than the convective time scale ($\Delta t \leq c/U$, herein called "fast"), and those which are slower than the convective time scale ($\Delta t \gg c/U$, herein called "slow"). Fast flow-field phenomena include the overriding convective flow, shear-layer instabilities and LEV burst point unsteadiness. Conversely, slow flow-field

phenomena include LEV burst-point motion and viscously-driven events such as the onset of surface separation.

Along this same vein, the analysis of Grismer and Jenkins¹¹ and the models of Myatt⁸ and Graham¹⁴ assumed that the unsteady rolling moment of the 65° delta wing undergoing harmonic and ramp-and-hold motions could be divided into two components. The first component was given by the potential flow about the wing. This component may be calculated using any potential-flow solver, such as the panel code QUADPAN¹⁵ or the vortex-lattice methods in HASC95,¹⁶ using the instantaneous position and rates for the conditions of interest. Given the physics assumed for this component, it constituted the fast-acting component of the aerodynamic response and reacted with the instantaneous roll angle and rate with no history effects.

The second component was found by subtracting the potential flow component from the total unsteady rolling-moment response. This “vortical” component of the rolling moment was assumed to be the result of the spanwise-differential surface pressure on the upper surface due to asymmetric LEV burst point locations at non-zero body-axis roll angles. The vortical component from constant-rate-ramp-and-hold motions were used to evaluate the vortical component’s time constant by fitting a lagged-network⁸ or exponentially-building curve¹¹ to these data. Grismer and Jenkins¹¹ and Myatt’s⁸ analyses found that time constants much greater than one were consistently found when LEV burst was present over the planform, while $\tau \cong 1$ corresponded well to conditions devoid of LEV burst. Such a correspondence was not surprising given that vortex burst is generally slow to respond to wing motion or control inputs.¹³

Theoretically, as disturbances of arbitrary frequency reach the delta wing’s (or any other body’s) near flow field, the flow field structure will react in a manner consistent with its time scale. If the time scale is sufficiently slow compared to that of the disturbance, the disturbance will pass before the flow field may react. Therefore, any disturbance to such a flow field will impart a pressure disturbance onto the wing which has an attenuated high-frequency ($fc/2U > 1$) component. The flow field in this example behaves as a physical low-pass filter.¹⁷ Conversely, flow field structures with fast time scales will have the ability to react to the convective disturbances without this attenuation. Furthermore, should the model undergo an unsteady motion, the aerodynamic response will be characteristic of the flow field’s ability to adapt to the disturbance to the boundary conditions.

Finally, if the time scale should change due to a sudden change in the flow field’s fundamental structure, *i.e.*, a bifurcation in its topology, this change may be apparent in the spectra of the aerodynamic response. Such a change would amount to changing the band-width of the filter, thereby changing the spectra. It follows that if a critical state is encountered which changes the flow field’s time constant, such a shift in the spectra ought to be observed.

This hypothesis may be verified by performing an adequate frequency analysis on the time histories of static load data. Note that this step is different from observing the RMS of these signals in that it is the frequency content of this “noise” and not its mean amplitude that is of interest.

3.3 HCAR Experiment

Figures 6 – 8 present time-averaged rolling moment coefficient data from the three body-axis angle of attacks used in this study. Normal force and pitching moment data similarly showed nonlinear and even non-analytic behavior,⁷ but are omitted from this discussion for brevity.

These data were taken using an exceptionally-fine resolution in roll angle (0.36°). These data and their analysis were described thoroughly in Reference 7. Uncertainty analysis for these data found that the 95% confidence interval, based on the standard deviation of the mean of the 5000 data samples, was well contained in the size of the symbols which represent the experimental data.

In each data set, a number of locations where the data undergo a discontinuous change in value or slope were readily apparent. The nonanalytic nature of these discrete locations was confirmed through regression analysis. In Figures 6 – 8 the regression results from attempting to fit a single, nonlinear function of Legendre polynomials to 23rd order to the entirety of data are shown. Figures 9 –11 present the results of breaking the regression curve at the critical states (marked by the vertical lines). The full-range results clearly do not represent the data throughout their entirety, emphasizing locations where the data appears to change discontinuously. The broken fits show vast improvement over the full-range results. Each of these critical states was associated with a change in the topology of the skin-friction lines on the upper surface.⁷

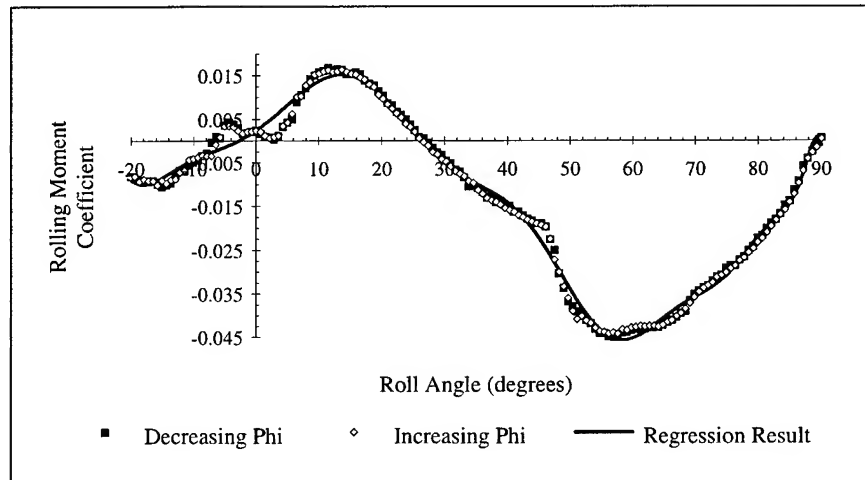


Figure 6 Static rolling moment coefficient as a function of roll angle with full-range regression results, $\sigma = 25^\circ$.

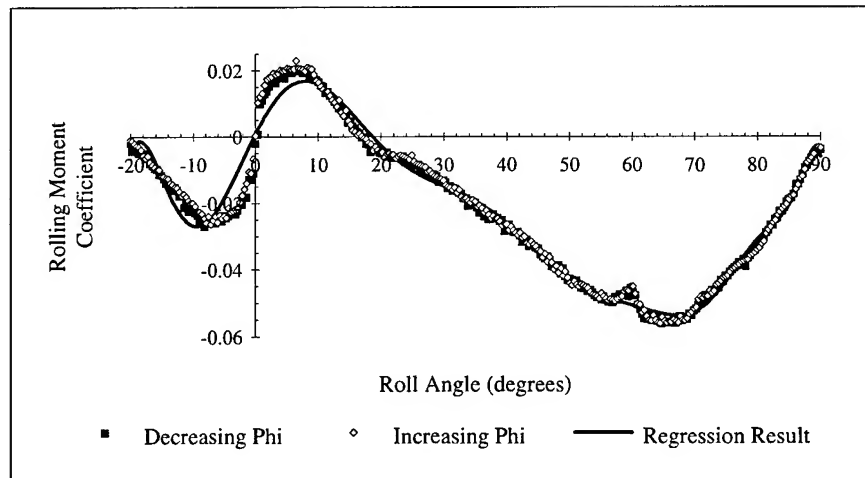


Figure 7 Static rolling moment coefficient as a function of roll angle with full-range regression results, $\sigma = 30^\circ$.

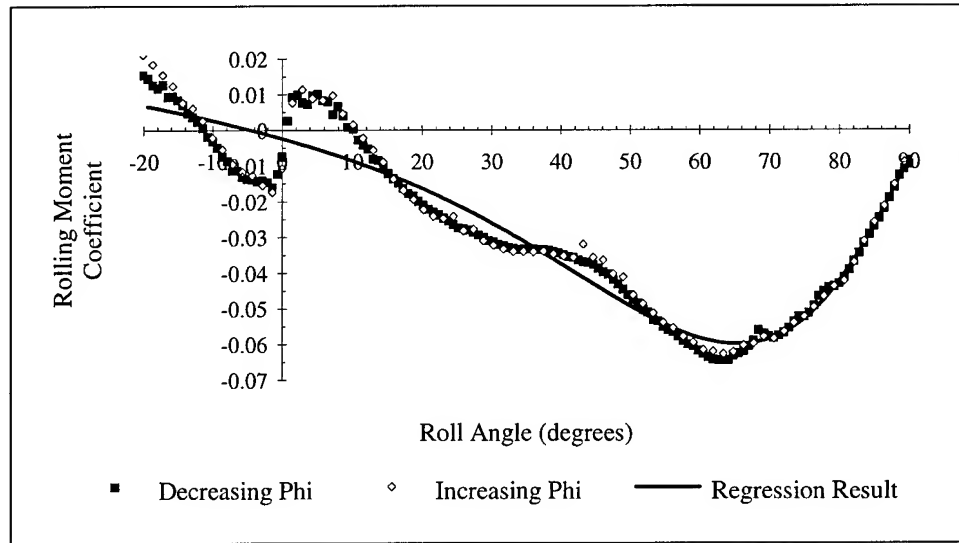


Figure 8 Static rolling moment coefficient as a function of roll angle with full-range regression results, $\sigma = 35^\circ$.

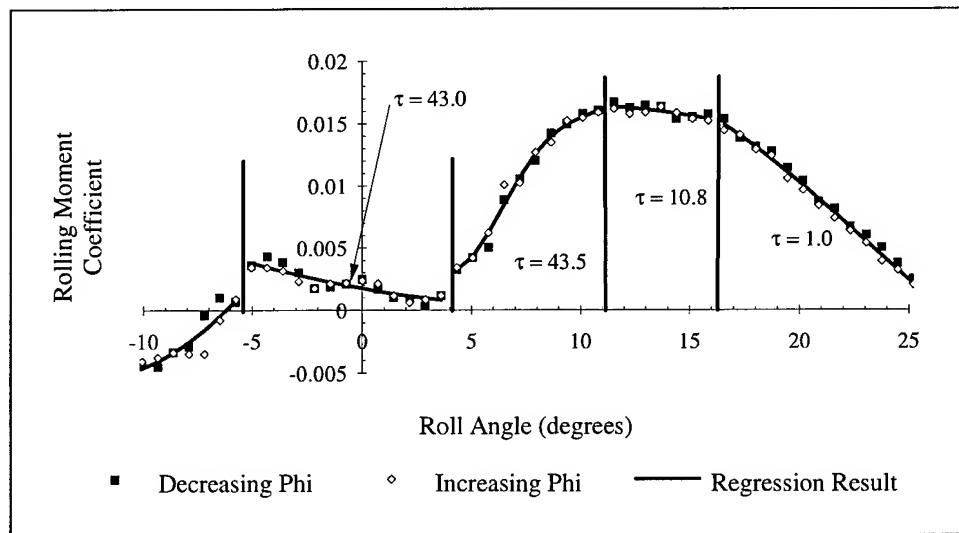


Figure 9 Static rolling moment coefficient as a function of roll angle showing critical state locations and unsteady response time constants, $\sigma = 25^\circ$.

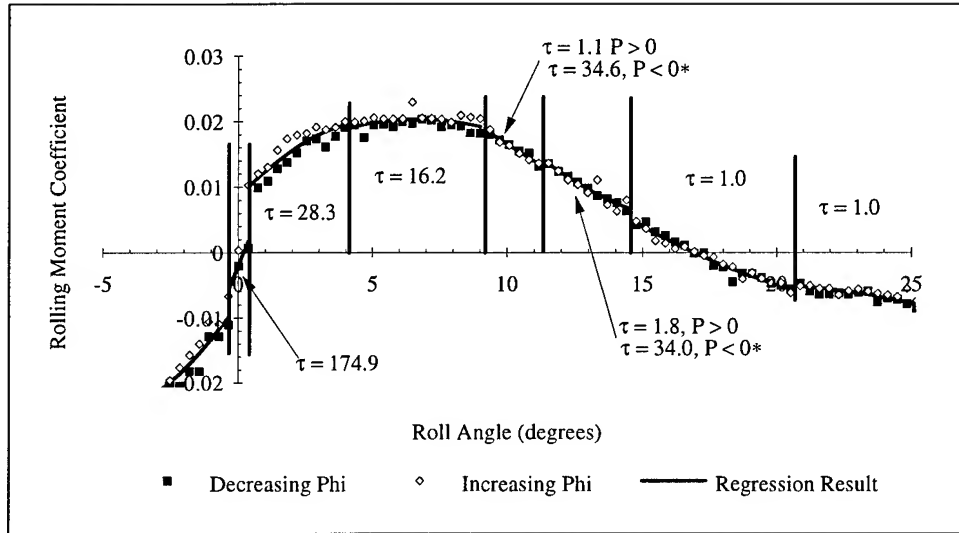


Figure 10 Static rolling moment coefficient as a function of roll angle showing critical state locations and unsteady response time constants, $\sigma = 30^\circ$.

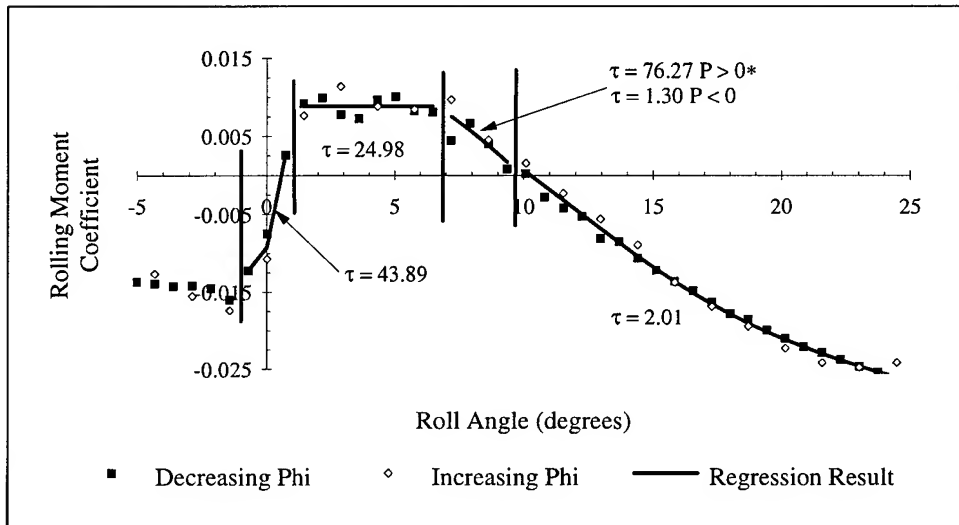


Figure 11 Static rolling moment coefficient as a function of roll angle showing critical state locations and unsteady response time constants, $\sigma = 35^\circ$.

The predominant time scales of the flow structures present were determined by conducting constant-rate ramp motions for ranges of roll angle where no critical states were present. Within the unsteady rolling moment response, a convective time scale response component ($\Delta t U/c \cong 1$) and a single lagged time scale ($\Delta t U/c \gg 1$) were assumed. The lagged-response model of Myatt⁸ was used to determine the lagged time constant of the unsteady rolling moment via an interval-halving optimization procedure. This procedure is more thoroughly discussed in Reference 7.

Summaries of the time constants found in each roll angle region (for $\phi < 20^\circ$) between critical states is summarized in Figures 9 - 11, superimposed onto the static force and moment data. Note that for all three body-axis angles of attack, the lagged time constant τ was greatest

within those regions closest to $\phi = 0^\circ$ and approached 1 as ϕ exceeded 10° to 15° . In three regions, τ was dependent on the direction and rate of the motion ($P > 0$ indicating an increasing roll angle). In all other regions, other than $-0.4^\circ < \phi < 0.4^\circ$ at $\sigma = 30^\circ$, the time constant was within 10% of the mean value shown regardless of rate ($0.0005 \leq P \leq 0.005$), direction or displacement of the ramp motion. The asterisks following some numbers indicate that the values had a rate dependence which was greater than 10 percent of the indicated average.

The complete time histories of the static rolling moment signals from roll angles of -18° to 90° in increments of 3.6° and from -10.1° to 15.1° in increments of 0.72° were decomposed via the PSD and autocorrelation methods. The non-dimensionalizing of time by the semispan – proper for lateral flight mechanical quantities – gave results on the same order with the convective time scales as the span and root chord lengths were nearly equal.

The first example of these results, from $\sigma = 30^\circ$, $\phi = 32.4^\circ$ (Figure 12), shows that in the lower frequency bands the unsteady rolling moments were quiescent at this condition, similar to the SARL result shown in Figure 5. These results were typical of the other force and moment components at this condition as well.

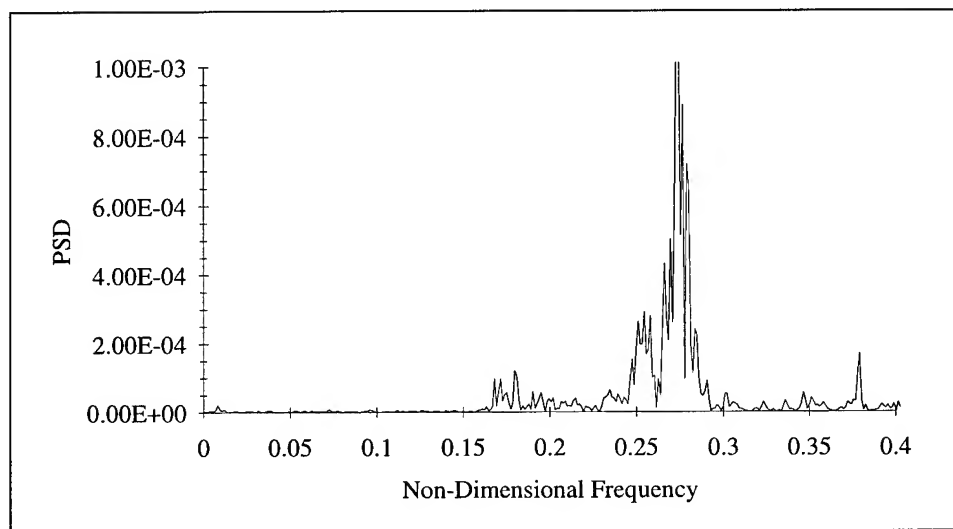


**Figure 12 Power spectral density decomposition of time series rolling moment data,
 $\sigma = 30^\circ$, $\phi = 32.4^\circ$.**

The large, relatively wide-band spikes between nondimensional frequencies of 0.2 to 0.3 (20 – 30 Hz) seen in Figure 12 were seen throughout these reduced data, a fact which was initially quite troubling. In discussions with colleagues¹⁸ at HCAR, it was found that similar spectral results had been found in other HCAR facilities with great consistency. It is believed that at least part of this contamination of the signal was a result of either mechanical vibrations within the laboratory building or seismic vibrations from the nearby power and steam plant and was not solely the subharmonic of electromagnetic noise.

At other conditions, the low-frequency content of the aerodynamic response was seen to rise. Figures 13 and 14 contain data from $\phi = 10.1^\circ$ and 0.0° at $\sigma = 30^\circ$, respectively. Interestingly, results from the former case was of a wider band and slightly higher frequency. The significance of this shifting in frequency, whether this result reflects physical reality or was the result of the inaccuracy of the discrete FFT¹⁹, was not determined.

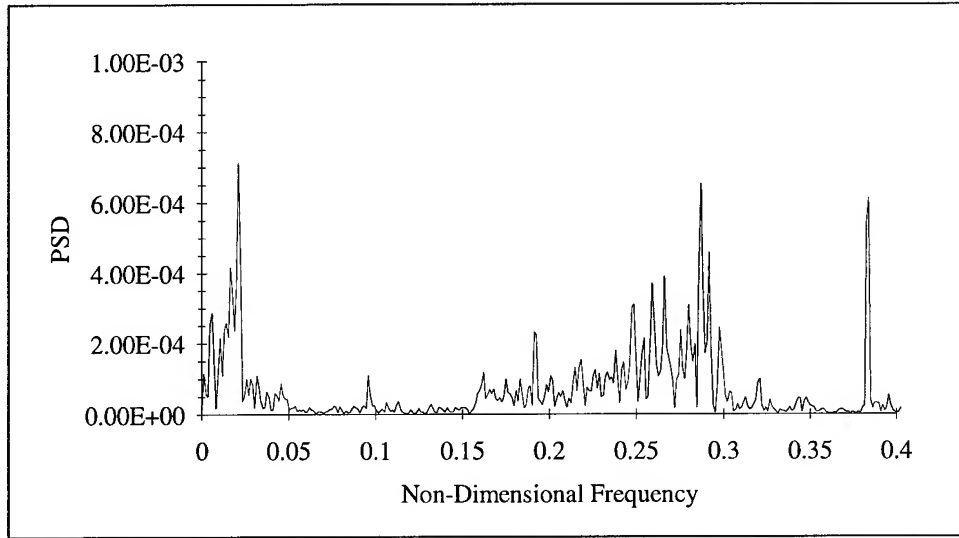


**Figure 13 Power spectral density decomposition of time series rolling moment data,
 $\sigma = 30^\circ$, $\phi = 10.1^\circ$.**

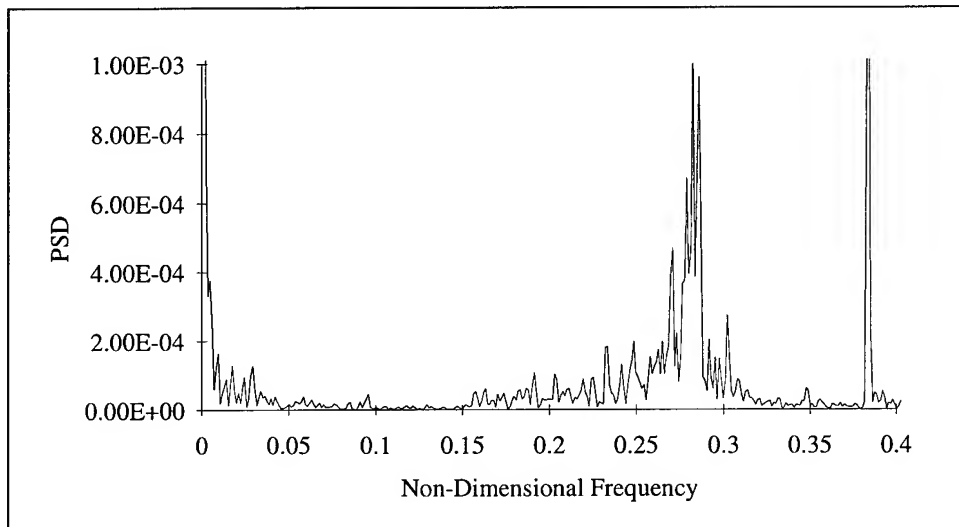


**Figure 14 Power spectral density decomposition of time series rolling moment data,
 $\sigma = 30^\circ$, $\phi = 0.0^\circ$.**

As a more broadly-based, although admittedly crude, comparison of these data's low-frequency content, a quantitative measure of this content was devised. Using a trapezoidal-rule integration, the PSD results were integrated with respect to frequency for non-dimensional frequencies less than 0.1. Obviously, the greater the integrated value, the larger the overall low-frequency content. This measure was found to be more reliable than tracking the peaks at individual frequencies, as the local peaks were not consistently at a single or handful of specific frequencies.

The integrated-PSD results from $\sigma = 25^\circ$ (Figure 15) showed a broad extent of low-frequency magnitude, but with multiple local minima and maxima. Given the presence of LEV burst over the planform near 60% c_r at $\phi = 0^\circ$,⁷ the hypothesized correspondence between low-frequency

content and the presence of LEV burst⁹ appears to be contradicted. The spectra contained little low-frequency content near $\phi = 0^\circ$, and only once the leeward LEV burst point crossed the trailing edge into the wake did this segment of the spectra show a significant increase. On the other hand, note that changes in the trends of low-frequency content with roll angle did correspond to critical state locations (indicated by the vertical lines), although this parameter did not change discontinuously with a critical state encounter. A second, broader (with respect to range in roll angle) peak formed between $\phi = 25^\circ$ and 52° . These critical states corresponded to conditions where the windward LEV burst point moved toward the trailing edge with increasing roll angle (as a result of the effective angles of attack and sweep at these conditions²⁰), and two unrelated bifurcations occurred in secondary flow structures.⁷

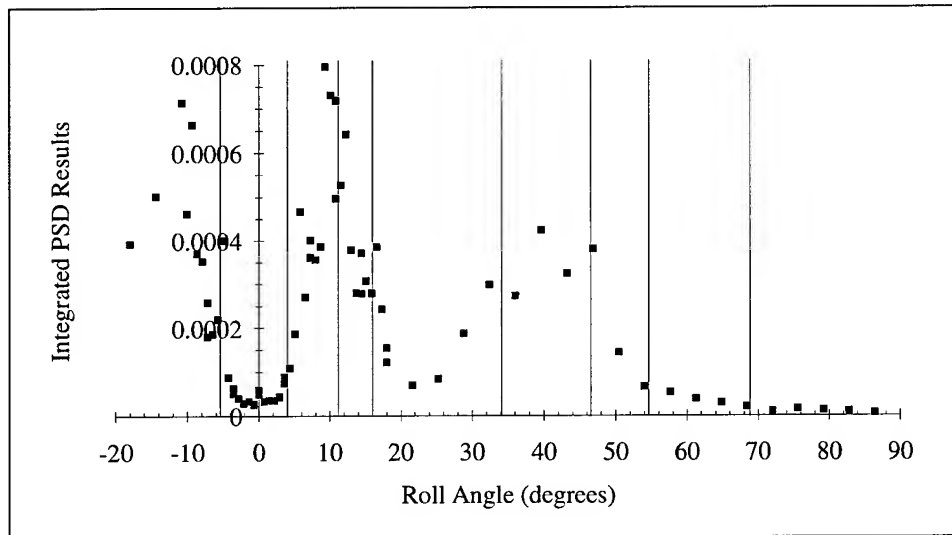


Figure 15 Integrated low-frequency PSD results, $\sigma = 25^\circ$.

Three clearly defined regions can be seen in the integrated-PSD results from $\sigma = 30^\circ$ as shown in Figure 16. For $\phi < 15^\circ$, the low-frequency content was the greatest, a 3- to 4-fold increase, on average, from that immediately outside of this range. It was in this region where the leeward LEV burst point was approaching the trailing edge. The rapid change in the integrated parameter corresponded closely to the critical state at $\phi = 14.3^\circ$ found through the regression analysis. Note that this increase in low-frequency content was not associated with the transition of the leeward LEV burst point across the trailing edge *per se*; instead, the low-frequency content appeared to dissipate as the leeward burst point traveled further from the trailing edge with increasing roll deflection.⁷ The final region within these data existed for $\phi > 60^\circ$, where the value of the parameter fell by a further factor of four from the intermediate range. The location of this fall-off was again near a critical state, this one at $\phi = 60.3^\circ$. This critical state was associated with the decomposition of the weak windward LEV into multiple streamwise vortices which originated along the leading edge.

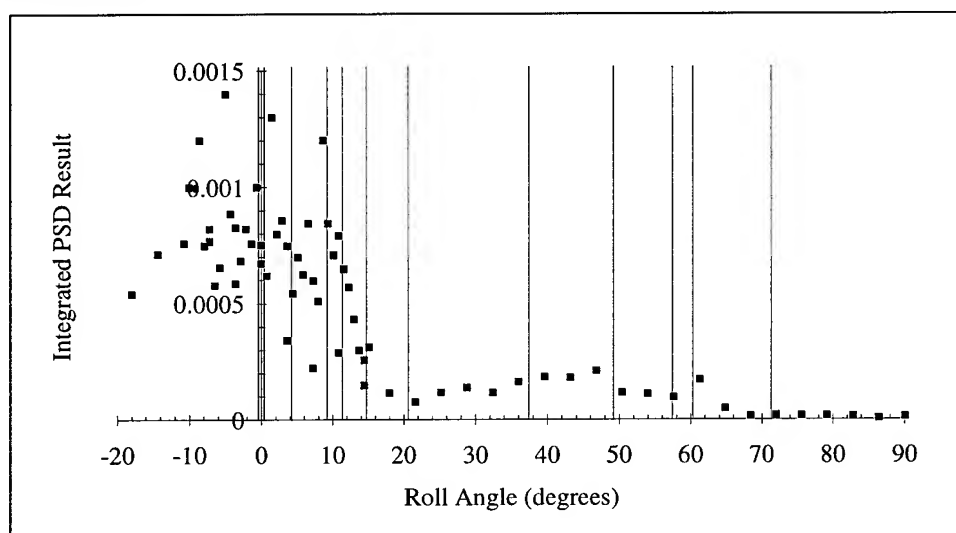


Figure 16 Integrated low-frequency PSD results, $\sigma = 30^\circ$

Results from the spectral analysis for $\sigma = 35^\circ$ data were similar to the result for $\sigma = 30^\circ$. The band of roll angles for which the low-frequency content was significantly above the background was narrower than that seen at $\sigma = 30^\circ$, but this region contained significantly greater signal power. These results are reflected in Figure 17 which displays the integrated PSD results from this condition. The LEV burst points did not contain considerable unsteadiness and did not cross the trailing edge until a $\phi \cong 42^\circ$; therefore, it was unlikely that this low-frequency content was due to LEV burst. Instead, unsteadiness seen indirectly in the skin-friction line results at very low roll angles (indicative of flow instability or time variance), spiraling turbulent flow aft of LEV burst, and large regions of stalled flow along the windward leading edge may all be suspected in causing this result.

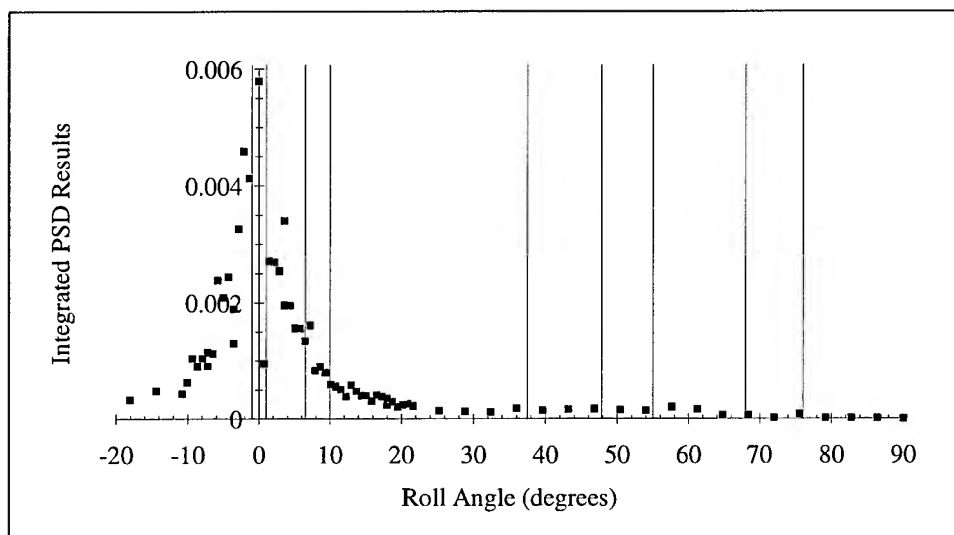


Figure 17 Integrated low-frequency PSD results, $\sigma = 35^\circ$.

An autocorrelation analysis was also performed on these data. Although the autocorrelation results were not conclusive, they were consistent with periodic data with superimposed wide-band noise when compared to the examples of Bendat and Piersol²¹.

3.4 Discussion of Results

From the results in the above sections, the nature of the unsteady aerodynamic response, the presence of critical states and the spectra of the static data may be compared. In comparing the unsteady aerodynamic time constants shown in Figures 9 through 11 with the measure of the low-frequency content in Figures 15 through 17, significant evidence confirming the relationship between the changes in the rolling moment's low-frequency spectra and the presence of critical states is shown.

Changes in the low-frequency content, as measured through the integration of the PSD with respect to the frequency below nondimensional frequencies of 0.1, did not appear to happen discontinuously. Instead, this parameter changed relatively smoothly, with the critical state typically appearing somewhere during the transition from one plateau or peak to the adjacent minima. Such a result suggests that the change in the spectra, and thus the change in the stability of the flow structure which leads to its bifurcation, occurs gradually with respect to roll angle.

Not all critical states were seen to effect changes in the spectra. In particular, those critical states between $-11^\circ < \phi < 11^\circ$ at $\sigma = 30^\circ$ caused no observable variation in the integrated parameter. However, the shift in the spectra seen in Figs. 13 and 14 may indicate a more subtle change with these critical states. Further data acquisition and analysis are required to explore this possibility.

Contrary to the opening hypothesis, these results show that the presence of an elevated low-frequency portion of the spectra did not always correspond to conditions where a lagged unsteady aerodynamic response occurred. In particular, at $\sigma = 25^\circ$ between $-4^\circ < \phi < 4^\circ$, a lagged response was present but the integrated PSD parameter entered into a lull in this same range. However, the critical states on either side of this lull corresponded well to the rapid increases in this value with increasing roll angle magnitude. Furthermore, since no unsteady motions were conducted for $\phi > 30^\circ$ at any of the inclination angles, a statement regarding whether additional conditions where slow responses were present cannot be made. This omission includes $\sigma = 25^\circ$, $\phi \cong 40^\circ$, where the integration parameter experiences a local peak and the windward LEV was relatively strong (as determined from surface oil flow results⁷).

The presence of elevated low-frequency spectra did not always correspond to the presence of the LEV burst point over the wing. Both the $\sigma = 25^\circ$ and 35° data demonstrate this contradiction to earlier conclusions.⁹ From the results of Addington,⁷ at $\sigma = 25^\circ$, the LEV burst point crossed the leeward trailing edge at approximately $\phi = 4^\circ - 6^\circ$, and persisted over the windward wing until its dissolution into discrete feeding-sheet vortices at approximately $\phi = 48^\circ$. At $\sigma = 35^\circ$, the leeward LEV did not cross the trailing edge until approximately $\phi = 38^\circ$. At both conditions, if the presence of the LEV burst point were responsible for the elevated low-frequency spectra, the persistence of these spectra would have been much greater. Furthermore, the lull in their presence between the 5° critical states at $\sigma = 25^\circ$ also would not exist if the hypothesized relationship between the burst point location and low-frequency content were true. Hence, although burst point may play a role in determining whether the spectra has an elevated low-frequency content, it cannot be the only factor.

Given that the presence of LEV burst does not directly correspond to the presence of the low-frequency spectra, a physical explanation for this phenomena is not readily apparent. Additional data are required in order to understand the physical mechanisms involved.

3.5 Summary

The results of a study into the relationship of the low-frequency spectra of static rolling moment data and the presence of critical states in the aerodynamic response data of a 65° delta wing have been presented. Through these results, it does appear that many, but not all, critical states correspond to changes in the low-frequency content of the static rolling moment spectra. These spectra did not change discontinuously with the critical-state encounter; instead, the critical state was typically found to reside at conditions where the spectra was in transition from being greatly elevated above the background noise to being of the same order of the background noise. Furthermore, it was found that the presence of LEV burst did not necessarily elevate the levels of the low-frequency content. It was also found that the presence of elevated low-frequency spectral content often, but not always, corresponded to conditions where the unsteady aerodynamic response was slow in reaching new equilibrium values following wing motion.

Given that the elevation in the low-frequency bands did not correspond directly to the presence of LEV burst, the issue of what causes this elevation must be addressed. This issue is proposed as the subject of future research.

Finally, despite the lack of full understanding of the physics of this relationship, the correspondence between the critical state locations in roll and changes in the low-frequency content of the static rolling moment's spectra does offer promise in the economical detection of some critical states.

4.0 Static Slope Analysis

This section reports a correlation which has been observed repeatedly in these 65° delta wing data. This correlation is between the static slope of the rolling moment coefficient, the slope of the static response as predicted using potential-flow-based methods, and the magnitude of the unsteady response time constant. Should this correlation prove to be more than mere coincidence, it would be a useful tool for locating flight conditions which may possess undesirable unsteady aerodynamic response characteristics. The data used in this discussion were acquired in two different wind tunnel tests using similar 65° delta wing geometries, shown in Figures 3 and 4.

4.1 Calculation of Potential and Vortical Flow Contributions in the Experimental Data

The appearance of multiple time scales in the unsteady rolling moment data suggests the separation of this response into at least two components. Myatt,⁸ modifying the approach used by Grismer and Jenkins,¹¹ assumed that the unsteady response consisted of four components acting over two potentially-disparate time scales.

The first two components were assumed to be linear functions of the instantaneous roll angle and roll rate, thereby providing the fast-time-scale response. Myatt⁸ modeled these components by using the results of a paneling code run using the geometric conditions of the SARL wind tunnel experiments. At small to moderate roll angles ($\phi < 25^\circ$), these results were approximately linear with roll angle and could thus be reduced to linear stability derivatives.

The remaining two components were assumed to be functions of the angle and rate time histories by way of a lag-network transfer function.¹⁷ These components were free to act over much longer time scales (although they were not constrained to do so). For the complete details on how the lag-network time constants were calculated, the interested reader is referred to Reference 8.

4.2 Calculation of the Numerical Prediction

A numerical prediction for the static rolling moment was provided by HASC95,²² an engineering-level stability-and-control prediction code. HASC95 uses a vortex-lattice methodology for calculating the potential flow about the body of interest, with semi-empirical corrections included for high-angle-of-attack conditions.

For this analysis, the 65° delta-wing geometry was entered into HASC95 as a simple two-panel grid with accurate accounting for the leading- and trailing-edge bevels but not including the center body. Flow separation and LEV vortex effects were toggled off, so that only the attached-flow contribution to the aerodynamic forces and moments would be included. The implications for removing the LEV effects will be discussed in the following sections.

4.3 Correlation Between Experimental and Numerical Static Slopes

Available for this analysis were data from two wind tunnel tests, both of which used body-axis roll angle as the independent variable of interest. In spite of using different models and freestream velocities (100 m/s in SARL, 14.7 m/s at Notre Dame), these experiments resulted in data with similar characteristics. Most importantly, both data sets contained numerous critical states which separated regions of roll angles with different unsteady-response time constants.

In Figures 18 - 20, the static rolling moment coefficients (symbols) are presented as functions of the static roll angle. Superimposed on these data is the rolling moment as calculated by HASC95 (denoted by the solid line), the locations of the critical states (solid vertical bars), and the unsteady-response time constant (τ) values. The time constants are presented having been nondimensionalized by the semispan and freestream velocity. As the span and root chord of these models were nearly equal, one nondimensional time unit is approximately one convective time unit ($c_{root}/2U$).

The first of the data presented (Figure 18) are from wind tunnel experiments conducted in the SARL wind tunnel at WPAFB. The unsteady-response time constants shown with these data are those found by Myatt.⁸ These data were collected using the model shown in Figure 3 with the body-axis angle of attack fixed at 30° .

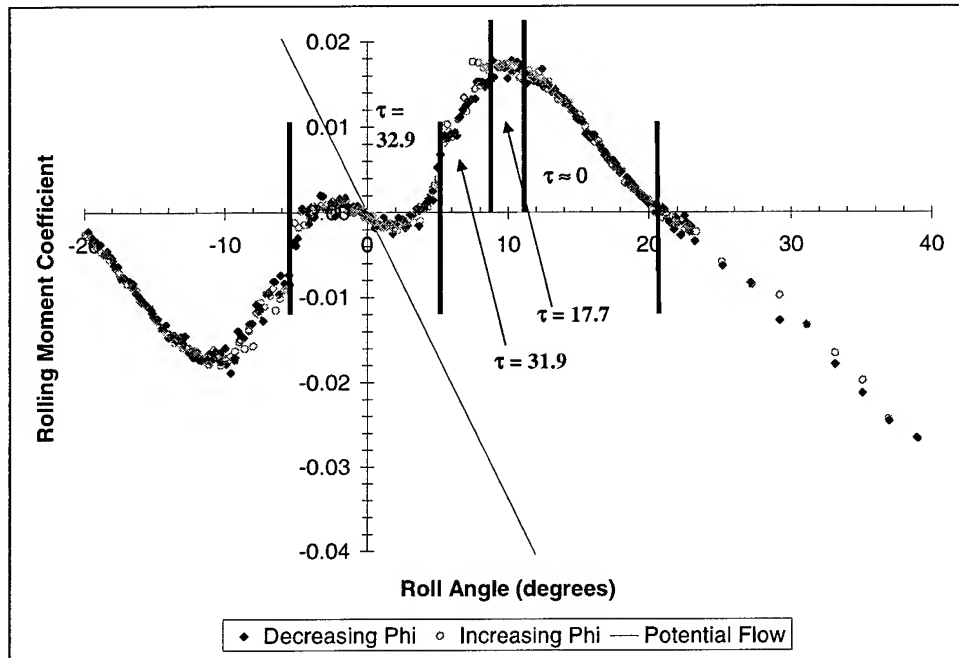


Figure 18 Static rolling moment data from the SARL wind tunnel with the potential flow prediction, critical state locations and unsteady-response time constants. $U_\infty=100\text{m/s}$, $\sigma=30^\circ$

Figures 19 – 21 present data from Addington⁷ for fixed body-axis angles of attack of 25° , 30° and 35° , respectively. These data were acquired at the University of Notre Dame's Hessert Center for Aerospace Research in a 0.6m – by – 0.6m, subsonic wind tunnel using the model shown in Figure 4. The time constants were calculated using the state-space model developed by Myatt.⁸

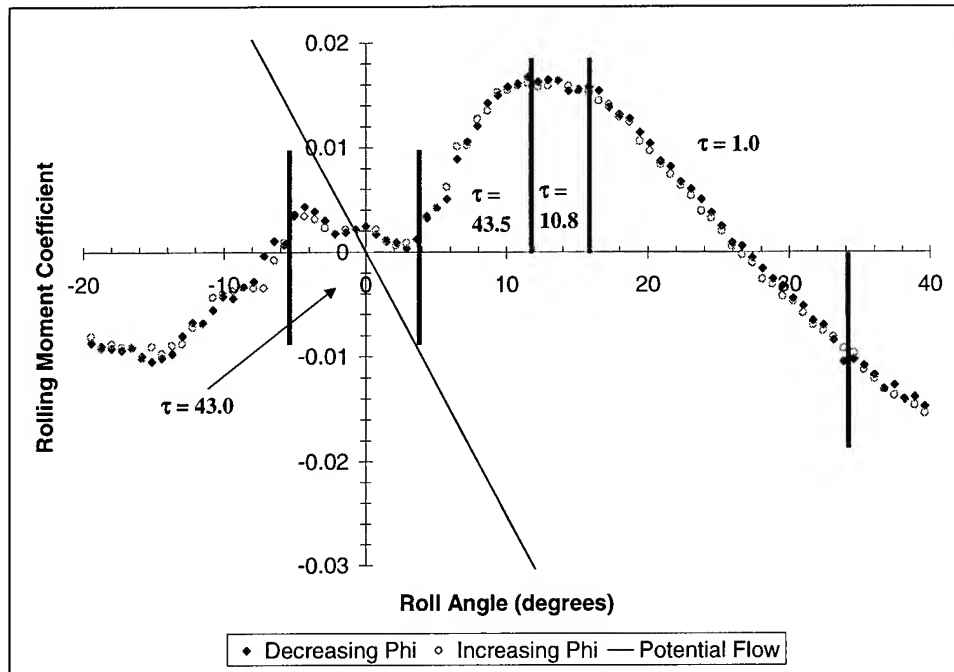


Figure 19 Static rolling moment data from the University of Notre Dame wind tunnel with the potential flow prediction, critical state locations and unsteady-response time constants.
 $U_{\infty} = 14.7 \text{ m/s}$, $\sigma = 25^{\circ}$.

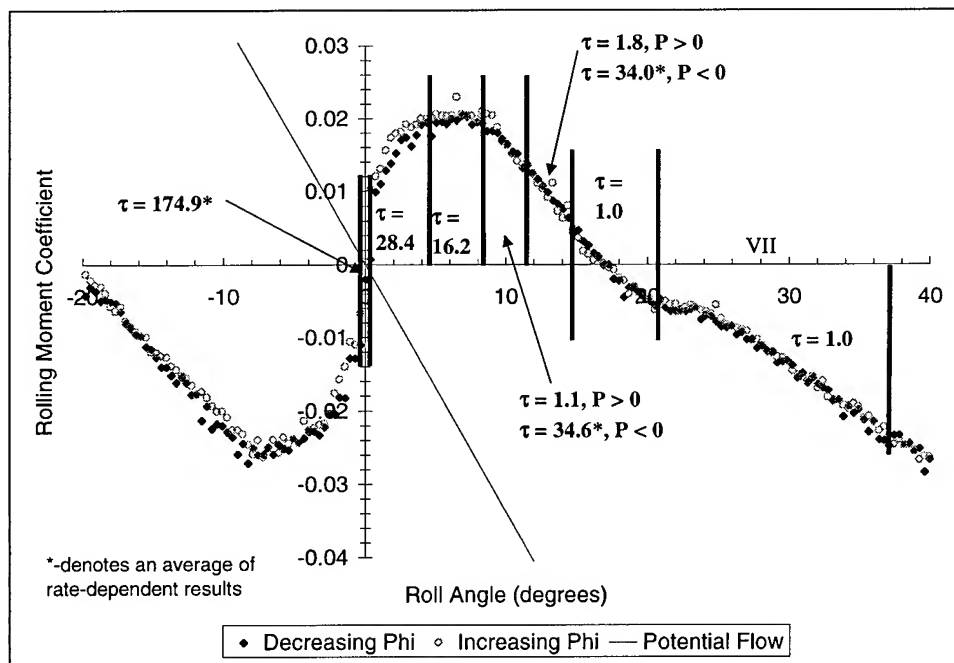


Figure 20 Static rolling moment data from the University of Notre Dame wind tunnel with the potential flow prediction, critical state locations and unsteady-response time constants.
 $U_{\infty} = 14.7 \text{ m/s}$, $\sigma = 30^{\circ}$.

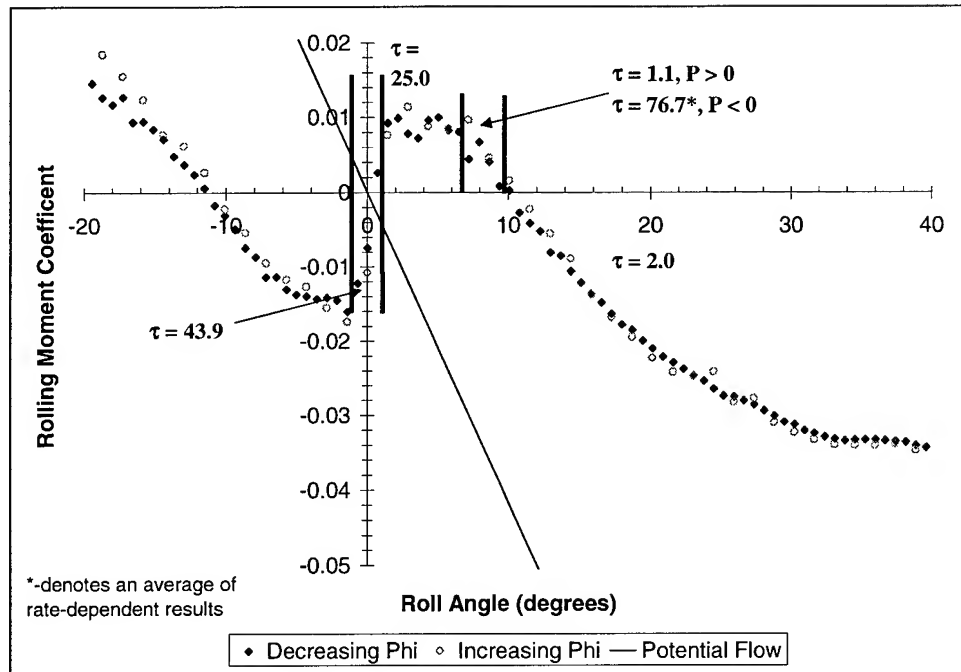


Figure 21 Static rolling moment data from the University of Notre Dame wind tunnel with the potential flow prediction, critical state locations and unsteady-response time constants.
 $U_{\infty} = 14.7 \text{ m/s}$, $\sigma = 35^{\circ}$.

4.4 Correlation of Static Slope Comparability and Critical State Locations

Jenkins³ was the first to compare the static slopes of the experimental data and potential-flow prediction to the unsteady-response characteristics. As can be seen in Figure 18, in those regions between adjacent critical states where the slope of the static wind tunnel data was relatively constant and similar to that of the potential flow calculations, the unsteady response time constant was on the order of zero or one. Time constants of this order indicated that the unsteady rolling moment was not lagged in this region. On the other hand, if the slope varied between critical states (as it did between the $|\phi| \approx 5^{\circ}$ critical states shown in Fig. 3) or differed greatly from that of the potential flow calculation, the time constant was greater than one by at least one order of magnitude. Such time constants were indicative of the type of responses shown in Figure 2.

This same relationship can be seen in the data shown in Figures 19 – 21. Furthermore, these data highlight a related trend: the greater the deviation of the slopes, the greater the value of the time constant. This trend was particularly noticeable in Figures 20 and 21, where the slopes of the static data near $\phi = 0^{\circ}$ were steep and positive, and the time constants were larger than in adjacent regions where the slope was near zero.

The correlation was less well defined in the later data than in the SARL data. First, three distinct regions where the unsteady-response time constant was a function of the direction of the roll motion were found. The physical cause for this result has not been determined. In all three cases, however, the magnitude of the lagged component of the response was small, and the overall response was very nearly instantaneous.

An additional instance where this correlation was less well defined was in the 35°

inclination angle data. For roll angles greater than 10° , the slope of these data was not constant with respect to roll angle, instead possessing an upward concavity. However, the unsteady rolling moment response maintained a time constant of 2.0 throughout this roll angle range with minimal deviation. Within this region, the leeward LEV burst point was present over the planform, but its position was less sensitive to roll angle than the other conditions. (At $\sigma = 35^\circ$, the burst point moved only 2% root chord per degree roll angle displacement, while the sensitivity at $\sigma = 25^\circ$ and 30° was 7% - 10% c_{root} per degree. These details are included in Ref.7.) Therefore, the small-amplitude (5° - 10°) motions used in this study did not cause large LEV burst point displacements, leaving the greater increment to the faster potential-flow component.

4.5 Discussion of Results

The results presented above demonstrate that a degree of correlation does exist between the similarity of the static experimental data and potential-flow prediction slopes and the unsteady rolling moment response time constants. This qualitative result was far from perfect, but the trend was repeatable across a number of test conditions and facilities. In summary, when the slopes of the potential-flow-based prediction and the experimental data between adjacent critical states were of the same order, the time constant was usually of order zero to one, indicating a "fast" response. Conversely, when these slopes were not of the same order or varied between the bordering critical states, the time constants were much greater than one, indicating a response containing a lagged component. Moreover, as the difference between the two slopes grew, the unsteady-response time constant increased in magnitude.

The physical cause of this relationship appears to lie in the behavior of the LEV burst points. Huang and Hanff²³ have shown that the asymmetric suction provided by the burst points, when they are over the planform and sufficiently downstream of the apex (*i.e.*, the spanwise center of pressure has a large moment arm), provided a destabilizing rolling moment which overwhelmed the remaining aerodynamic influences. On the other hand, when the burst points were either in the wake or near the apex of the delta wing, other influences on the rolling moment remained: the coherent leeward LEV, and the flow over the wing's lower surface. A coherent LEV's strength is primarily a function of angle of attack,²⁴ the value of which at the leading edge being given by $\tan^{-1}(\tan(\sigma)\tan(\phi))$ for the rolled delta wing.²³ Because this parameter changed very little for small roll angles in the angle-of-attack range discussed herein, the coherent leeward LEV's strength would have been nearly invariant with roll angle. Since the flow on the lower surface was attached and its separation point fixed at the sharp leading edge, potential flow models were able to capture the associated flow physics to first order.

Many researchers, as summarized by Rockwell,¹³ have noted that the LEV burst points respond to wing maneuvers and other unsteady conditions over time scales much slower than convection. Huang and Hanff²³ further demonstrated that the lag in the aerodynamic response was directly associated with this lagged behavior of the LEV burst point motion. Given this relationship, the existence of the lagged component of the unsteady rolling moment is not surprising. Naturally, this type of response would result at the same conditions where the static rolling moment exhibits the destabilizing effect of asymmetric LEV burst point positions. Conversely, the unburst LEV and lower-surface flows were of the types to respond to unsteady conditions with convective time scales.¹³ In the absence of any other "slow" flow field structure, either in the equilibrium flows or resulting from a rate-induced flow field topological bifurcation, the dominance of these flows in determining the rolling moment would suggest a fast unsteady response.

Of concern is the offset of the potential-flow prediction and the experimental data. The omission of the leeward LEV's contribution to the rolling moment is the likely primary cause of this offset. The influence of the leeward LEV would be to add a destabilizing rolling moment increment, which is consistent with the offset seen in these comparisons. This increment may be calculated using the potential flow models of Arena,²⁵ or the leading-edge suction analogy of Polhous.²⁶ However, the more simple potential flow model used here demonstrated the basic premise of this study: by comparing a simple numerical model for the flow to the experimental results, the fundamental nature of the unsteady aerodynamic response may be assessed.

Furthermore, since the most rapid assessment of the potential for nonlinear unsteady effects was desired, the removal of the more complicated methods of Arena²⁵ and Polhomus,²⁶ for which no “off-the-shelf” numerical codes are known to this author, were omitted. Therefore, for the purposes of this illustration, the more complicated aerodynamic model was not used.

An additional concern is the use of potential flow theory at conditions where its validity is tenuous. Since potential flow is based on linear theory, the assumptions involved become invalid at large roll angle deflections. The reasonable agreement between the static slopes comes in spite of the large perturbations to the flow field and the presence of stalled flow. To fully assess the validity of this comparison, data of a similar nature but acquired at much lower angles of attack and roll are required.

In spite of these concerns, the repeatability of this correspondence provides an intriguing possibility for predicting whether the flows which generate critical states contained lagged effects without acquiring large volumes of dynamic data. The applicability of this relationship is naturally dependent on the flow physics involved. For example, should both the fast- and slow-acting aerodynamic effects provide components of similar trend with the independent variable (*e.g.*, are both stabilizing or destabilizing), such a relationship would be far more difficult to discern. On the other hand, for configurations which elicit vortex-dominated flows similar to those found about delta wings, such as slender bodies, forebodies and planforms with leading-edge extensions, the applicability of this comparison appears significant.

4.6 Extrapolation of Results to Other Flows

To further illustrate the utility of this analysis method, the classic example of a two-dimensional airfoil oscillating in pitch will be discussed. The lift generated by such a hypothetical geometry is shown in Figure 22 as a function of angle of attack for static conditions. If the airfoil is sufficiently thin, potential flow models the aerodynamic lift generated with reasonable to exceptional accuracy until trailing-edge flow separation – a viscous phenomenon – occurs. Given that this event represents a change in the flow field topology, it may be considered a critical state.

Oscillating such an airfoil in pitch results in two very different types of responses, depending on whether the critical state is crossed. For the motion which does not cross the critical state, the response is linear, characterized by the classic stability equation $C_L = C_{L\alpha} \alpha(t) + C_{Lq} q(t)$, where q is the instantaneous pitch rate. This response is readily calculated numerically using potential flow models. On the other hand, motions which cross the critical state elicit a much different type of response,²⁷ as is shown for the notional case in Figure 23. This response, often referred to as “dynamic lift” or “dynamic stall,” is characterized by a hysteresis in lift (and pitching moment), as is shown by the solid curve in Figure 23. (The separation between the two notional dynamic examples is exaggerated from typical numerical and experimental results here for clarity.) Unlike the linear response, this response cannot be simulated using potential flow models, as it involves separated and vortical flows. The initial rise in lift follows that of the potential case to first order, but lift declines precipitously following the shedding of the accumulated vorticity in a large-scale vortex (the “dynamic stall vortex”). Lift then undershoots the potential flow prediction (and the static value) significantly during the downstroke as the flow remains separated from the upper surface well below the static stall angle of attack. Lift does not typically meet up with the potential-flow prediction once flow reattaches to the upper surface, either at the end of the downstroke or at very low angles of attack.

Note that the different types of aerodynamic responses may be separated by the location at which the potential flow model for the static response fails: the critical state. At angles of attack below that of the critical state, linear models for the instantaneous lift are more than sufficient to the task. On the other hand, crossing the critical state introduces nonlinearities which necessitate a more complex modeling methodology. This result follows from the result of modeling the static lift in Figure 22; the potential flow model's inability to predict static stall is a demonstration of its inability to model the increasingly-important (and nonlinear) viscous effects. There is no reason for one to expect that the linear model ought to be adequate for the dynamic case if the static physics are not adequately modeled.

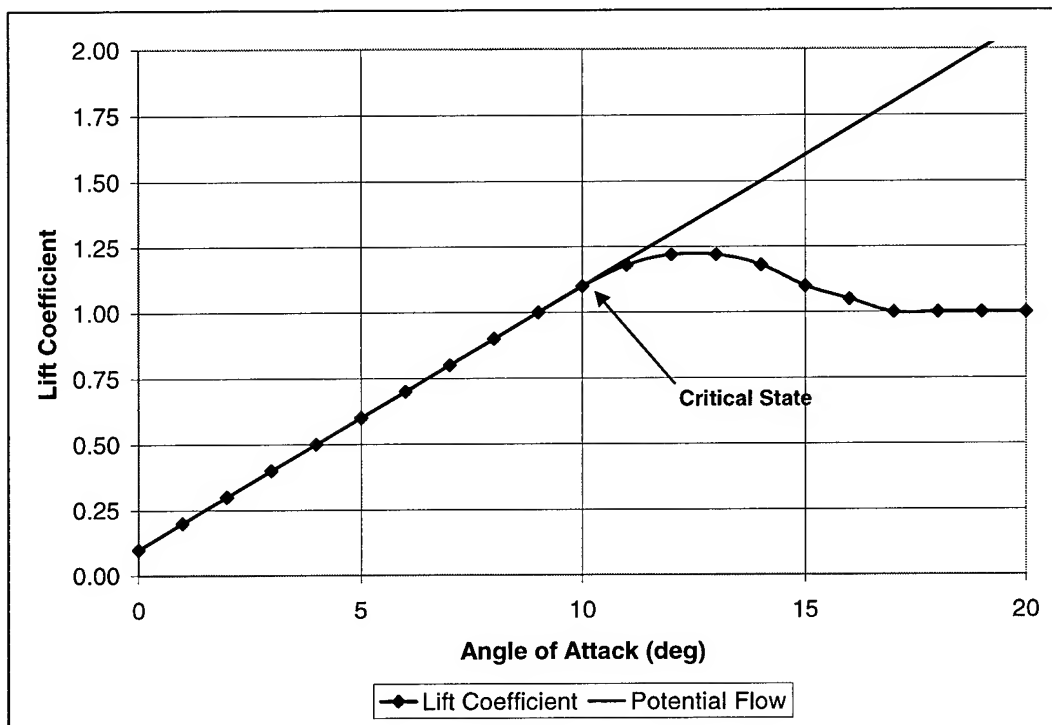


Figure 22 A notional comparison of the static lift generated by a thin two-dimensional airfoil compared to a potential flow prediction.

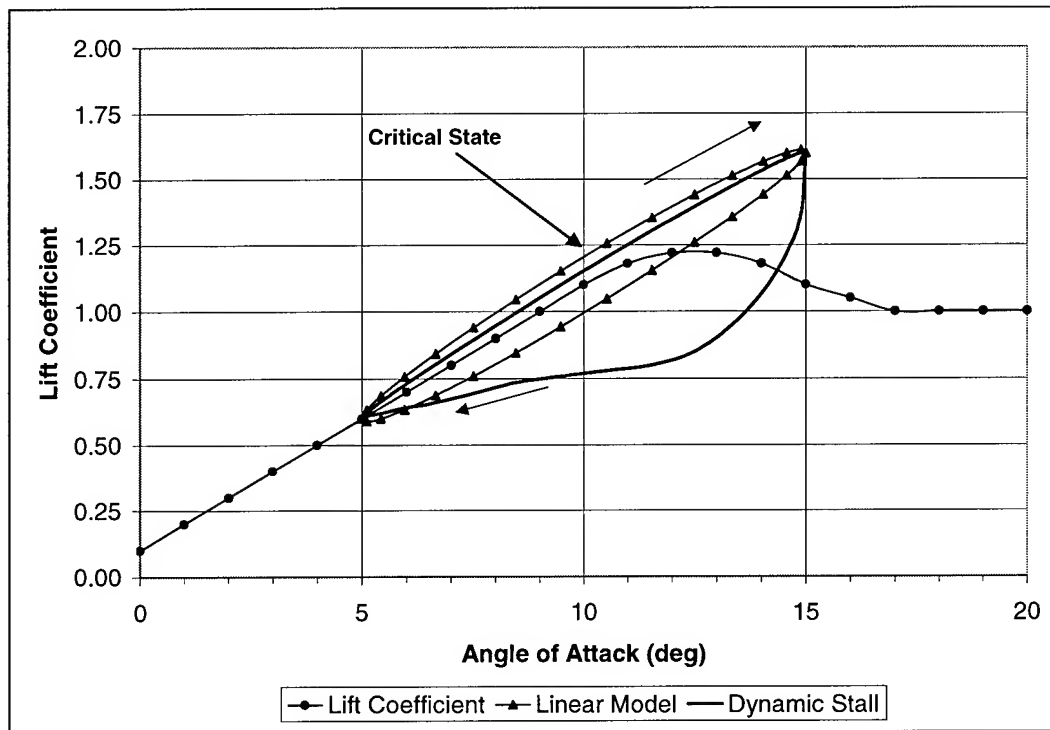


Figure 23 A notional example of the dynamic lift generated by a harmonically-oscillating two-dimensional airfoil.

4.7 Summary

Data acquired using 65° delta wings at high angles of attack have shown a correlation between the slopes of the experimental and potential-flow-based predictions of the static rolling moment and the unsteady rolling moment response to body-axis rolling motions. The physical cause appears to lie in the behavior of the LEV burst points. Although the applicability of this comparison has to be proven for full aircraft configurations, its usefulness in predicting whether the unsteady aerodynamic response of configurations eliciting delta-wing-like flows which contain lagged components appears significant. The usefulness of this procedure was also demonstrated for a two-dimensional example, suggesting that other types of flows may similarly benefit from this analysis.

5.0 Conclusions and Recommendations

The results presented in this report demonstrate that the careful analysis of aerodynamic data can provide insight into the location and effects of critical states within the test envelope without resorting to extensive experimentation. In both cases, the procedures require little if any additional data and relatively little additional time or computational power to execute, yet provide significant insight into the relevant flow physics. Should these procedures prove useful on other configurations and in other facilities, the time and cost savings could prove immense.

6.0 References

- ¹ Chambers, J.R., "Independent Consultant Activities in Support of the NASA/DOD Abrupt Wing Stall (AWS) Program: Task 2 – Historical Review of Wing Drop," Ball Aerospace Systems Division, September 1998.
- ² Jenkins, J.E., and E.S. Hanff, "Highlights of the IAR/WL Delta Wing Program," presented at Workshop III - Delta Wings: Unsteady Aerodynamics and Modeling, AIAA Atmospheric Flight Conference, 8 August 1995.
- ³ Jenkins, J.E., "Nonlinear Aerodynamic Characteristics of a 65 Degree Delta Wing in Rolling Motion: Implications to Testing and Flight Mechanics," AIAA Paper 97-0742, January 1997.
- ⁴ Tobak, M., and G.T. Chapman, "Nonlinear Problems in Flight Dynamics Involving Aerodynamic Bifurcations," AGARD CP 386, Paper 25, May 1985.
- ⁵ Tobak, M., G.T. Chapman, and A. Ünal, "Modeling Aerodynamic Discontinuities and Onset of Chaos in Flight Dynamical Systems," *Extrait des Annales des Telecommunications*, Tome 42, May - June 1987, pp. 300-14.
- ⁶ Jenkins, J.E., and J.H. Myatt, "Modeling Nonlinear Aerodynamic Loads for Aircraft Stability and Control Analysis," AGARD Workshop on Stability in Aerospace Systems, May 1992.
- ⁷ Addington, G.A. The Role of Flow Field Structure in Determining the Aerodynamic Response of a Delta Wing, Ph.D. Dissertation, University of Notre Dame, April 1998; see also Addington, G.A., and R.C. Nelson, "The Correspondence Between Flow-Field Structure and Critical States on a 65-Degree Delta Wing," AIAA Paper 98-4520, August 1998.
- ⁸ Myatt, J.H., Modeling the Rolling Moment on the 65-Degree Delta Wing for Rolling Motions at High Angle of Attack, Ph.D. Thesis, Stanford University, April 1997; see also Myatt, J.H., "A Nonlinear Indicial Response Model for the Rolling 65-Degree Delta Wing," AIAA Paper 96-3406, July 1997.
- ⁹ Jenkins, J.E., J.H. Myatt, and E.S. Hanff, "Body-Axis Rolling Motion Critical States of a 65-Degree Delta Wing," *AIAA J. Aircraft*, Vol. 33 No. 2, 1996, pp. 268-78. See also Jenkins, J.E., J.H. Myatt, and E.S. Hanff, "Body-Axis Rolling Motion Critical States of a 65-Degree Delta Wing," AIAA Paper 93-0621, January 1993.
- ¹⁰ Jobe, C.E., A.H. Hsia, J.E. Jenkins, and G.A. Addington, "Critical States and Flow Topology on a 65° Delta Wing," *AIAA J. Aircraft*, Vol. 33 No. 2, 1996, pp. 347-352.
- ¹¹ Grismer, D.S., and J.E. Jenkins, "Critical-State Transients for a Rolling 65° Delta Wing," AIAA Paper 96-2432, June 1996.
- ¹² Brendel, R.G., T.J. Mueller and A.F. Huber II, "The Flow Quality of Subsonic Wind Tunnels with Atmospheric Exhaust," University of Notre Dame, 1986.
- ¹³ Rockwell, D., "Three-Dimensional Flow Structure on Delta Wings at High Angle-of-Attack: Experimental Concepts and Issues," AIAA Paper 93-0550, January 1993.
- ¹⁴ Graham, G.M., and J.E. Jenkins, "Semi-Empirical Indicial Response Model for 65° Delta Wing Oscillating in Roll," AIAA Paper 97-0326, January 1997.

-
- ¹⁵ Youngren, H.H., E.E. Bouchard, and R.M. Coopersmith, Quadrilateral Element Panel Method: Users' Manual, Ver. 3.2, Lockheed LR 30563, Burbank, CA, 1984.
- ¹⁶ Albright, A.E., C.J. Dixon and M.C. Hegedus, Modification and Validation of Conceptual Design Aerodynamic Prediction Method HASC95 with VTXCHN, NASA CR 4712, March 1996.
- ¹⁷ Ogata, K., Modern Control Engineering, 2nd ed., Prentice Hall, Englewood Cliffs NJ, 1990.
- ¹⁸ Minniti, R.J., III, and J.P. Wojno, Private Communications, June 1997.
- ¹⁹ *c.f.*, Bergland, G.D., "A Guided Tour of the Fast Fourier Transform," *IEEE Spectrum*, Vol. 6, July 1969, pp. 41-52.
- ²⁰ Addington, G.A., and Nelson, R.C., "The Predictability of Skin-Friction Line Topology on a Rolled Delta Wing", AIAA Paper 98-4352, August, 1998.
- ²¹ Bendat, J.S., and A.G. Piersol, Random Data: Analysis and Measurement Procedures, 2nd ed., Wiley, NY, 1986.
- ²² Albright, A.E., C.J. Dixon and M.C. Hegedus, Modification and Validation of Conceptual Design Aerodynamic Prediction Method HASC95 with VTXCHN, NASA CR 4712, March 1996.
- ²³ Huang, X.Z., and Hanff, E.S., "Roll-Induced Cross Loads on a Delta Wing at High Incidence," AIAA Paper 91-3223, Sept. 1991.
- ²⁴ Lee, M., and C.-M. Ho, "Lift Force on Delta Wings," *ASME Applied Mechanics Review*, Vol. 43 No. 9, September 1990, pp. 209-221.
- ²⁵ Arena, A.S., Jr., An Experimental and Computational Investigation of Slender Wings Undergoing Wing Rock, Ph.D. Dissertation, University of Notre Dame, April 1992.
- ²⁶ Pohlomus E.C., A Concept of the Vortex Lift of Sharp-Edged Delta Wings Based on a Leading-Edge Suction Analogy, NASA TN D-3767, December 1966.
- ²⁷ Reynolds, G.A., and L.W. Carr, "Review of Unsteady, Driven, Separated Flows," AIAA Paper 85-0527, January 1985.